This document is the accepted manuscript version of the following article:
Liu, J., Wang, S., Kravchyk, K., Ibáñez, M., Krumeich, F., Widmer, R., … Cabot, A. (2018). SnP nanocrystals as anode materials for Na-ion batteries. Journal of Materials Chemistry A, 6(23), 10958-10966. https://doi.org/10.1039/c8ta01492b

Journal Name

ARTICLE

SnP nanocrystals as anode material for Na-ion battery

Junfeng Liu,[‡a] Shutao Wang,[‡bc] Kostiantyn Kravchyk,*[bc] Maria Ibáñez,[bc] Frank Krumeich,[b] Roland Widmer,[d] Déspina Nasiou,[e] Michaela Meyns,*[a] Jordi Llorca,[f] Jordi Arbiol,[eg] Maksym V. Kovalenko,[bc] Andreu Cabot*[ag]

Received 00th January 20xx,
Accepted 00th January 20xx

DOI: 10.1039/x0xx00000x

www.rsc.org/

Tin monophosphide is a layered material consisting of Sn-P-P-Sn sandwiches that are stacked on top of each other to form a three dimensional crystallographic structure. Its composition and crystal structure makes it an excellent candidate anode material for sodium-ion batteries (SIBs). However, SnP is yet to be explored for such and other applications due to its challenging synthesis. In the present work, we report the synthesis of SnP nanocrystals (NCs) from the reaction of hexamethylphosphorous triamide (HMPT) and a tin phosphonate prepared from tin oxalate and a long chain phosphonic acid. SnP NCs obtained from this reaction displayed spherical geometry and a trigonal crystallographic phase with a superstructure attributed to ordered diphosphorous pairs. Such NCs were mixed with carbon black and used as anode materials in SIBs. SIBs based on SnP NCs and sodium(I) bis(fluorosulfonyl)imide (NaFSI) electrolyte displayed high reversible capacities of 600 mA h g^{-1} at a current density of 100 mA g^{-1} and cycling stability for over 200 cycles. Their excellent cycling performance is associated to both the small size of the crystal domains and the particular composition and phase of SnP which prevent mechanical disintegration and major phase separation during sodiation and desodiation cycles. These results demonstrate SnP to be an attractive anode material for sodium ion batteries.

Introduction

The low cost and high abundance of sodium resources in the Earth crust make sodium-ion batteries (SIBs) a cost-effective alternative to lithium-ion batteries (LIBs) for large scale energy storage.[1,2] Having a similar operation mechanism, progress achieved for LIBs can be in large part transferred to SIBs. This is for instance the case for layered cathode materials developed for LIBS and applied in SIBs. However, the larger size of sodium has associated slower/unfavorable intercalation/alloying kinetics and larger volumetric changes that particularly affect the anode materials. In this regard, commercial graphite anodes used for LIBs are not suitable for SIBs. While graphite is readily lithiated to LiC_6, graphite intercalation compounds with high Na densities are energetically unfavorable.[3]

Phosphorous, tin, antimony and alloys based on these elements are among the best candidate anode materials for SIBs. These elements are able to alloy with sodium to reach high theoretical capacities.[4-7] In particular, elemental phosphorous has a very high theoretical capacity of 2596 mA h g^{-1} corresponding to the formation of Na_3P.[8-10] However, phosphorous has a limited electrical conductivity. Additionally, it displays a huge volumetric change of 490% during formation of the Na-rich phase. This extreme volume expansion results in pulverization and peeling off from the current collector, causing loss of electrical conductivity.

To overcome limitations of pure phosphorous and improve cycling performance, combinations of phosphorus with metals forming metal phosphides (M_xP_y), have been proposed, where M is inactive Co,[11-13] Ni,[14,15] Cu,[16,17] Fe[18-20] or electroactive Ge,[21,22] and Sn[23-35] with regard to Na. Superior performance of metal phosphides over pure phosphorous is manly attributed to the presence of metal atoms acting as electronic pathways drastically enhancing electronic conductivity.

Among them, tin phosphides, with two electroactive elements, have certainly attracted much attention as low-cost anode material for SIBs with high theoretical capacity, 1132 mAh g^{-1} for Sn_4P_3, associated with the formation of Na_3P and $Na_{15}Sn_4$.[23-35]

Besides, pure tin as anode material has shown excellent performance as anode material for Na-ion batteries.[36-40] But Sn has a much lower theoretical capacity 847 mA h g^{-1} compared with P, and it also exhibits poor cyclability due to the severe

[a.] *Catalonia Institute for Energy Research – IREC, 08930 Sant Adrià de Besòs, Barcelona, Spain*
[b.] *Institute of Inorganic Chemistry, Department of Chemistry and Applied Biosciences, ETH Zürich, Zürich, CH-8093,Switzerland*
[c.] *EMPA-Swiss Federal Laboratories for Materials Science and Technology, Dübendorf, CH-8600, Switzerland*
[d.] *Nanotech@surfaces Laboratory, EMPA-Swiss Federal Laboratories for Materials Science and Technology, CH-8600, Switzerland*
[e.] *Catalan Institute of Nanoscience and Nanotechnology (ICN2), CSIC and BIST, Campus UAB, Bellaterra, 08193 Barcelona, Catalonia, Spain*
[f.] *Institute of Energy Technologies, Department of Chemical Engineering and Barcelona Research Center in Multiscale Science and Engineering. Universitat Politècnica de Catalunya, EEBE, 08019 Barcelona, Spain*
[g.] *ICREA, Pg. Lluis Companys 23, 08010 Barcelona, Catalonia, Spain*
[‡.] These authors contributed equally.
* Corresponding authors: K. K. kravchyk@inorg.chem.ethz.ch; M. M. michaela.meyns@awi.de; A. C. acabot@irec.cat
† Electronic Supplementary Information (ESI) available: additional synthesis conditions, HRTEM, XPS and electrochemical characterization. See DOI: 10.1039/x0xx00000x

volume change up to 420% during sodiation and desodiation process, resulting pulverization of electrode and rapid degradation of capacity.[36,37]

Besides a proper composition of the active anode material, to alleviate the pulverization problem and improve the cycling performance, the use of nanostructured materials is crucial. Nanomaterials can reduce the accumulated stress during sodiation, even at high charge/discharge rates, thus potentially preventing mechanical disintegration. Nanomaterials can also enhance electron and ion transport when within a conductive matrix and at the same time improve the kinetics of sodium insertion/removal.[41,42]

Reliable strategies to produce metal phosphide nanocrystals (NCs) with controlled parameters are not yet well developed, at least not at the level of oxides and chalcogenides. Particularly challenging has been the synthesis of phosphides of main group metals such as Ga, In, Ge and Sn.[43-49] In the past, various synthetic approaches of tin phosphides were developed.[23-34] As an example, 200 nm Sn_4P_3 particles were synthesized in solution using tin(II) acetylacetonate and trioctylphosphine (TOP), and used as SIB anode reaching a capacity of 719.8 mA h g^{-1} in the initial cycle.[25] While demonstrating high capacity values and low redox potentials,[25,26] Sn_4P_3 showed poor cycling performance. Its moderate stability was related to mechanical disintegration, which may be aided by the fact that Sn_4P_3 desintegrated into $Na_{15}Sn_4$ and $3Na_3P$ during the initial sodiation and it did not form again during desodiation.

Alternative phosphorus-richer tin phosphides have higher theoretical mass capacities. However, due to the challenge that the synthesis of tin phosphide phases different from Sn_4P_3 has so far represented, just one phosphorus-rich tin phosphide, SnP_3, prepared by reactive ball milling of Sn, red phosphorus and carbon black has been tested as anode material for SIBs.[30]

A tin phosphide yet to be explored for a number of potential applications, including SIBs, is the monophosphide, SnP. SnP is a metastable tin phosphide phase, but displaying a large kinetic stability at temperatures below 500 °C.[50] SnP has a layered structure composed of Sn-P-P-Sn sandwiches stacked together to form a three-dimensional crystal.[51] Its layered structure, metallic character and stoichiometric composition, which provides a theoretical capacity of 1209 mA h g^{-1}, make SnP an excellent candidate anode material for SIBs. Actually, the existence of diphosphorus pairs in the SnP structure has already been demonstrated to prevent phase segregation during lithiation/delithiation cycles,[52] resulting in a superior stability in LIB anodes.

In this work, we present a reliable synthetic approach to produce SnP NCs making use of stable and safe metal precursors. We further test the performance and stability of these SnP NCs as anode material for SIBs.

Experimental

Chemicals: Tin(II) oxalate (98%), tin(II) acetylacetonate ($Sn(acac)_2$, 99.9%), bis[bis(trimethysilyl)amino]tin(II), tin(II) stearate (90%), oleylamine (OAm, >70%), 1-octadecene (ODE, 90%) were purchased from Sigma-Aldrich. n-Tetradecylphosphonic acid (TDPA, 97%) was purchased from PlasmaChem GmbH. n-Octadecylphosphonic acid (ODPA) was obtained from PCI synthesis. Hexamethylphosphorous triamide (HMPT, 97%) was bought from Alfa Aesar. Dimethoxyethane (DME, battery grade) was purchased from Novolyte technologies Inc. sodium(I) bis(fluorosulfonyl)imide (NaFSI, 99.7%) was purchased from Solvionic SA. carbon black (CB, Super C65) was bought from Timcal Ltd. carboxymethyl cellulose (CMC,Grade: 2200, Lot No. B1118282) was bought from Daicel Fine Chem Ltd. Glass microfiber separator (GF/D, Cat No.1823-257) was bought from Whatman plc. Cu foil (9µm) was purchased from MTI Corporation. Coin-type cells was bought from Hohsen Corp., Japan. Chloroform and ethanol were of analytical grade and obtained from various sources. All chemicals were used as received, without further purification. All syntheses were carried out applying standard airless techniques: reactions were carried out using a vacuum/argon gas Schlenk line; air and moisture-sensitive chemicals were stored and handled in an argon filled glovebox.

Synthesis of SnP NCs: *Caution: Because this procedure involves the high-temperature decomposition of a phosphorous precursor that can liberate toxic and flammable phosphine gas, the reaction should only be carried out by appropriately trained personnel using rigorously air-free conditions and the Schlenk line should be connected with gas absorption solutions.*

In a typical synthesis, 103 mg of tin oxalate (0.5 mmol), 139 mg of TDPA (0.5 mmol), 5 mL of OAm and 10 mL of ODE were introduced in a 50 mL three-necked flask containing a stir bar. The flask was also equipped with a thermocouple and its adapter, a Liebig condenser, and a septum. The reaction mixture was stirred and heated to 100 °C under vacuum for 60 min to remove air, water and low-boiling point impurities. The solution was then placed under argon, heated to 180 °C in 10 min, and maintained at this temperature for additional 30 min to obtain a clear and transparent solution. Afterward, the solution was further heated to 270 °C within 15 min. At this temperature, 0.200 mL of HMPT (1.15 mmol) was injected into the flask and the reaction was kept at this temperature for 60 min. The flask was allowed to cool to 200 °C by removing the heating mantle and then cooled rapidly to room temperature with a water bath. The contents of the reaction mixture were transferred into centrifuge tubes, followed by centrifugation at 5000 rpm (3200 g) for 5 min. The isolated powder was re-suspended using 1:3 (v:v) chloroform and ethanol and then centrifuged again. This entire process was repeated twice. Finally the powder was suspended in 5 mL of chloroform in a vial.

Ligand removal: At room temperature and under continuous stirring, 5 mL of an aqueous 1 M hydrazine hydrate solution were introduced into a flask containing ~20 mg of NCs in 5 mL of hexane. The mixture was stirred until the NCs moved from hexane to the aqueous phase. The product was further washed twice with hexane and ethanol and centrifuged at 3000 rpm. A nanopowder was collected after drying the precipitate at room temperature.

Characterization: The NCs size and shape were examined by transmission electron microscopy (TEM) using a ZEISS LIBRA 120, operating at 120 kV. High-resolution TEM (HRTEM) and annular dark field scanning TEM (ADF-STEM) images were obtained by using a field emission gun FEITM Tecnai F20 microscope with a point-to-point resolution of 0.19 nm at 200 kV equipped with an embedded Quantum Gatan Image filter (Quantum GIF) for spectrum imaging (SI) electron energy loss spectroscopy (EELS) analyses. Images have been analyzed by means of Gatan Digital Micrograph software. Scanning electron microscopy (SEM) analyses were done in a ZEISS Auriga microscope equipped with an energy dispersive X-ray spectroscopy (EDS) detector operating at 20 kV that allowed studying composition. Ex situ EDS maps were collected on a FEI Talos F200X microscope operated at 200 kV. For SEM characterization, the materials were dispersed in chloroform and drop casted on silicon substrates. Powder X-ray diffraction (XRD) patterns were collected directly from the as-synthesized NCs dropped on Si(501) substrate with a Bruker AXS D8 Advance X-ray diffractometer with Ni-filtered (2 μm thickness) Cu Kα radiation (λ = 1.5406 Å) operating at 40 kV and 40 mA. A LynxEye linear position-sensitive detector was used in reflection geometry. X-ray photoelectron spectroscopy (XPS) was carried out on a SPECS system equipped with an Al anode XR50 source operating at 150 mW and a Phoibos 150 MCD-9 detector. Ex situ XPS measurements were carried out in normal emission using a monochromatized Al Ka X-ray radiation source and a Scienta R3000 display analyzer. Fourier transform infrared (FTIR) spectra were acquired using a PerkinElmer FTIR 2000 spectrophotometer. Spectra were recorded from 400 cm^{-1} to 4000 cm^{-1}.

Electrode fabrication, cell assembly and electrochemical measurements: Electrodes were prepared by mixing SnP NCs (64 wt%) with CB (21 wt%), CMC (15 wt%) and water using a planetary ball-mill (500 rpm, 1h). The resulting aqueous slurries were coated on Cu foil current collectors and then dried at 80 °C for 12 h under vacuum. All electrochemical measurements were conducted in air-tight coin type cells assembled in an argon-filled glove box. Elemental sodium was employed as both reference and counter electrode. As electrolyte, 5 M NaFSI in DME was used. Glass fiber was used as separator. Galvanostatic cycling tests were carried out at room temperature on MPG2 multichannel workstation (BioLogic). Capacities were normalized by the mass of SnP.

Results and discussion

Tin phosphide NCs were prepared in solution by reacting HMPT with a source of tin at 250-270 °C. The reaction was carried out in an ODE solution containing TDPA and OAm, as detailed in the experimental section. Owing to the relatively low boiling point of the phosphorous precursor used, HMPT, this was injected at the reaction temperature. Heating up procedures, involving mixing all the reactants at room temperature and then heating up the solution to the reaction temperature, were not fully reproducible due to the partial loss of HMPT during the process.

To optimize the synthetic procedure, different tin precursors were initially tested (Fig. S1). In the reaction conditions applied, bis[bis(trimethysiyl)amino]tin resulted in particles with broad size and phase/composition distributions, including metallic Sn, Sn_4P_3 and SnP. Tin acetylacetonate resulted in a mixture of Sn and Sn_4P_3 phases. Tin stearate mainly yielded SnP particles, with just minor impurities of other phases. Among the different compounds tested, tin oxalate was the only one yielding pure phase SnP upon reaction with HMPT in the presence of a phosphonic acid and OAm. This experimental result and the advantageous stability, low cost and low toxicity of tin oxalate made us selecting this precursor as the most convenient one to continue this work.

The reaction temperature was limited by the low boiling point of HMPT. This limitation was especially severe for tin precursors with moderate reactivity, since during the reaction, the phosphorus precursor could partially leave the reaction mixture. At 250 °C, the SnP NCs produced from tin oxalate were highly aggregated in a raspberry-like fashion, with an average size of 8 nm and a low crystallinity (Fig. S2). Using tin oxalate, 270 °C was found to be the optimum temperature to produce well-dispersed SnP NCs with high crystallinity (Fig. 1).

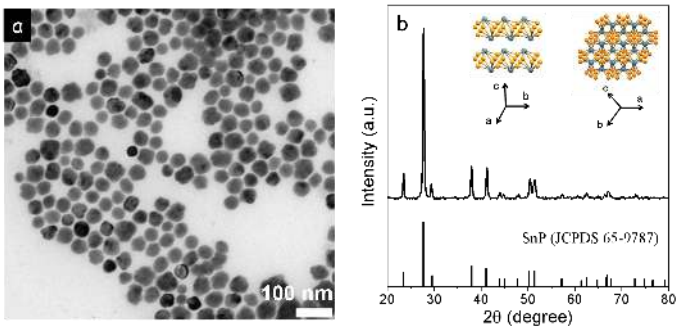

Fig. 1 TEM micrograph (a) and XRD pattern (b) of the NCs produced from the reaction of tin oxalate with HMPT at 270 °C. Reaction was carried out in ODE and in the presence of OAm and TDPA: TDPA/Sn = 1. Inset within the XRD graph shows the SnP crystal structure along two different directions.

To assess the role of TDPA, reactions with different amounts of this compound were carried out (Fig. S4). In the absence of TDPA, tin oxalate did not fully dissolve in the ODE-OAm solution. Thus, upon injection of HMPT, Sn_4P_3 particles with a drop-like morphology and sizes above 200 nm mixed with small amounts of metallic Sn were produced (Fig. S4a,e). Such morphology was similar to that obtained in a previous work from the reaction of tin(II) acetylacetonate with trioctylphosphine (TOP) at 350 °C.[25] In this previous work, tin(II) acetylacetonate was found to decompose to SnO, which was reduced to Sn and later reacted with TOP to yield Sn_4P_3.[25] In our reaction conditions, XRD and SEM-EDX analysis also demonstrated that in the absence of TDPA, tin oxalate initially decomposed to SnO, which later reacted with HMPT to yield Sn_4P_3 particles (Fig. S5 and S6).

With a TDPA/Sn ratio of 0.5, chains of aggregated NCs containing a blend of SnP and Sn phases were produced (Fig. S4b). Phosphonic acids strongly coordinate to tin, helping to dissolve the tin oxalate in the ODE solution. However, with a low amount of TDPA, part of the oxalate was not dissolved, and a mixture of phases was obtained. With a larger amount of TDPA, TDPA/Sn = 1, all the tin oxalate was well dissolved and a clear solution was obtained at 180 °C. After injecting HMPT, it took about 30 s for the color of the growth solution to change from colorless to black. The long nucleation time might be related to a strong binding of phosphonate to tin ions. Under these conditions, dispersed spherical 34 ± 5 nm NCs of pure SnP were obtained, and no extra phases were found from the XRD characterization (Fig. 1). The geometrical particle size matched well with the crystallographic size obtained from the Scherrer analysis of the XRD pattern, indicating a high crystallinity of the SnP NCs obtained. XRD characterization of the reaction product at different reaction times showed SnP to be directly produced from the reaction of the tin phosphonate complex and HMPT, with no intermediate phase forming (Fig. S10 and S11). No solid material was obtained before injecting HMPT. This XRD analysis also showed the NC crystallinity to improve with the reaction time (Fig. S10). When excess TDPA (TDPA/Sn =2) was used, no solid was formed after 1 h of reaction with HMPT.

The complex collected after mixing tin oxalate with TDPA at 180 °C was a white viscous compound with very low solubility in any organic solvent tested. These characteristics were similar to those of the compound formed using a cadmium precursor.[53,54] We thus hypothesize that the formed tin complex, most probably a tin tetradecylphosphonate, is a coordination polymer similar to cadmium octadecyl-phosphonate, which was identified as composed of layers of cadmium ions bridged together by phosphonate groups.[53,54]

Exchanging TDPA with a longer phosphonic acid, e.g. ODPA, maintaining otherwise identical conditions (ODPA/Sn =1, reaction temperature = 270 °C), resulted in smaller SnP NCs, with an average size of 23 ± 4 nm (Fig. S7 and S8). We ascribed this reduced NC size to a lower reactivity of the tin phosphonate complex formed from the longer chain phosphonic acid (ODPA) when compared with the shorter one (TDPA), as also observed for cadmium chalcogenides.[55]

In agreement with XRD patterns, HRTEM analysis showed NCs to have the trigonal SnP crystallographic phase (S.G.: P-3ml) with lattice parameters a = b = 4.3922 Å and c = 6.0400 Å (Fig. 2).[51] As described by J. Gullman, the SnP trigonal structure is formed by Sn octahedra filled with diphosphorous pairs that may have four different orientations (Fig. 2d).[51] In a perfect random distribution of the diphosphorous pairs orientations, no extra reflections should be observed in the power spectra (Fig. 2e). However, the power spectrum of several NCs showed streaky extra spots as those observed in Fig. 2b when visualizing the NC along the [10-10] zone axis. These streaky extra spots were in perfect agreement with the presence of stacking faults along the (0001) planes, i.e. in the sequence of the sandwiches composed of filled octahedral, as suggested by Y. Kim et al. [51,52] In other NCs, non-streaky extra spots were observed (red circles in fig. 2h, see also S12-S14) which indicated the presence of an ordered superstructure as hypothetically suggested by J. Gullman.[51] We attributed this superstructure to the ordered orientation of the diphosphorous pairs within the layers of filled octahedra. The structure model for a compound of the SnP type with the atomic pairs all oriented parallel with the c-axis was predicted by Hulliger,[56] but it was not previously experimentally reported.

Annular dark field scanning TEM (ADF-STEM) and STEM-EELS elemental composition maps revealed that Sn and P were uniformly distributed throughout each NC (Fig. 2k). SEM-EDS analysis showed that as-synthesized SnP NCs had an excess of phosphorous, P/Sn = 1.2 (Fig. S6), which we attributed to the presence of phosphonate as surface ligand.

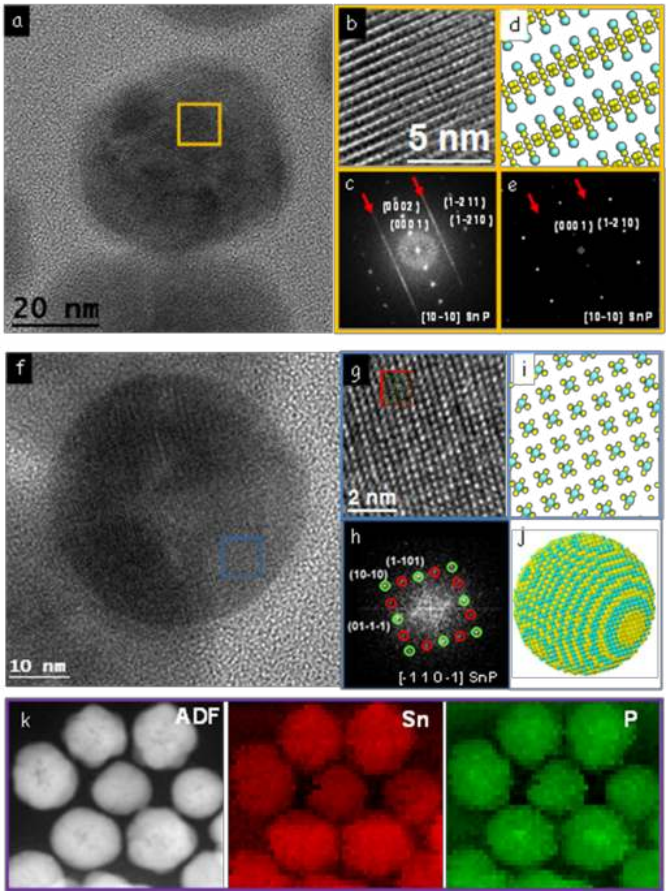

Fig. 2 a) HRTEM micrograph of a SnP NC with a trigonal structure. b-c) Magnified detail of the NC squared in orange (b) and its corresponding power spectrum (c). Stacking faults are revealed as the streaky extra spots (indicated by red arrows) in the power spectrum. d) Simulated SnP structure along the [10-10] zone axis showing all the possible diphosphorous pairs orientations occupied. e) Simulated electron diffraction for a disordered non-faulted crystal, where no streaky extra spots are observed. f) HRTEM micrograph of another SnP NC with the trigonal structure. g-h) Detail of the NC area squared in blue (g) and its corresponding power spectrum (h). In the power spectrum, some extra spots, which should not exist in the pure hexagonal structure, were found. These extra points, circled in red, could not be indexed by using the simple

trigonal SnP structure with a random distribution of the orientation of the diphosphorous pairs. Only the brightest spots from the FFT, circled in green, could be indexed. i) Atomic arrangement of the Sn (cyan) and the P (yellow) atoms in the SnP structure along the [-1 1 0 -1] zone axis including a random distribution of the diphosphorous pairs orientation. j) 3D atomic model of a 10 nm diameter SnP NC along the [-1 1 0 -1] zone axis. k) ADF-STEM micrograph and STEM-EELS elemental composition maps of several SnP NCs: Sn (red) and P (green).

The presence of a phosphonate surface ligand was confirmed by FTIR analysis (Fig. 3). The FTIR spectra of SnP NCs displayed peaks at 2922 and 2853 cm^{-1} attributed to the C-H stretching vibrations of alkyl groups of the tetradecylphosphonate group. For free TDPA, the vibrations associated to phosphorus are found in the region between 1200 and 900 cm^{-1}. Within this region, the absorbance band corresponding to the stretching of P=O (1167 cm^{-1}) and P-O bonds (1045, 985, and 952 cm^{-1}) can be localized. In the FTIR spectra of SnP NCs, these features were merged within a broad absorbance band centred at 1045 cm^{-1}. This band evidenced the presence of the phosphonate group while at the same time indicated a chemical alteration in the phosphonic acid head group which we assigned to its binding at the surface of NCs. After ligand removal, the absence of vibration modes of C-H, P=O and P-O bonds indicated that all phosphonate was removed by hydrazine hydrate.

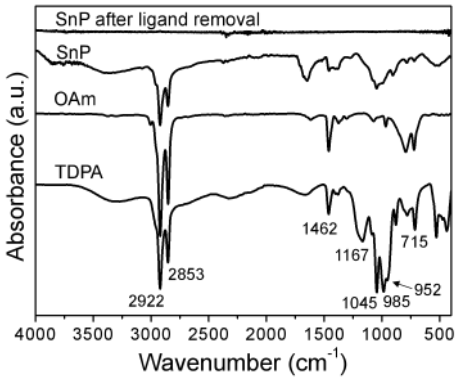

Fig. 3 FTIR spectra of TDPA, OAm and SnP NCs before and after ligand removal.

XPS analysis was used to characterize the chemical environment of atoms at the surface of SnP NCs (Fig. 4). Sn 3d electronic states were found at binding energies of 486.4 eV (Sn $3d_{5/2}$) and 494.9 eV (Sn $3d_{3/2}$), which suggested a SnO environment. In the P 2p region, three main distinct peaks were observed at 133.1 eV, 133.9 eV and 138.9 eV. The peak at 138.9 eV does not correspond to a P 2p electronic state but to Sn 4s electrons. On the other hand, the two main components at lower binding energies were assigned to the P $2p_{3/2}$ (133.1 eV) and P $2p_{1/2}$ (133.9 eV) electronic states of phosphorous in a phosphate chemical environment.[57] Minor peaks at 131.2 and 132.1 were associated to the metal-phosphide bond P-Sn in the hexagonal SnP structure, which represented a 10% of the total phosphorous detected at the NC surface.

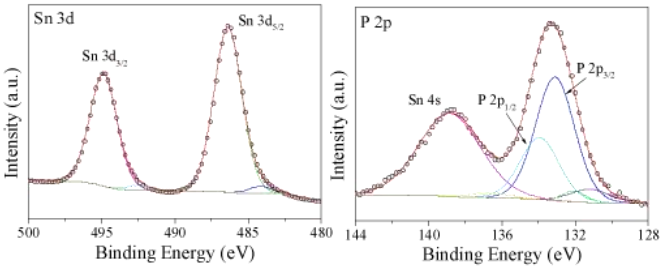

Fig. 4 XPS spectrum of the Sn 3d (left) and P 2p (right) regions obtained from SnP NCs. The Sn 3d spectrum was fitted with 4 peaks corresponding to 2 chemical states, matching the main one with the SnO binding energy (Sn $3d_{5/2}$ binding energy = 486.4 eV). Within the P 2p region, a band corresponding to Sn 4s electronic states is found. The P 2p band was fitted with four peaks, corresponding to 2 chemical states, matching the main one with the phosphate binding energy (P $3p_{3/2}$ binding energy = 133.1 eV).

EDX analysis of the NCs after ligand removal showed the phosphorous-to-tin ratio to be P/Sn = 0.96 ± 0.02. This phosphorous deficiency could be explained by considering a tin-rich surface after removal of the phosphate ligands. This deficiency was also consistent J. Gullman work, reporting SnP single crystals to have a significant amount of phosphorous vacancies and an overall stoichiometry: $SnP_{0.94}$.

For electrochemical measurements, SnP electrodes were prepared by mixing SnP NCs with CB, CMC and water, and casting the resulting slurries onto copper current collectors. Coin-type cells were employed for the electrochemical tests. The cell contained a sodium disk as counter and reference electrode, the SnP electrode as working electrode and a glass-fiber separator soaked with sodium electrolyte placed in-between both electrodes.

Fig. 5a shows cyclic voltammetry curves of the SnP electrodes at a scan rate of 0.1 mV s^{-1}. In the first cathodic cycle (sodiation step), a small broad peak at about 0.5-0.9 V *vs.* Na^+/Na was attributed to the formation of a solid electrolyte interphase (SEI) layer due to irreversible reduction of the electrolyte during the first cycle.[58,59] Upon further sodiation, a large reduction peak at 0.07 V *vs.* Na^+/Na aroused, which was ascribed to sodium insertion in SnP forming Na-Sn alloy and sodium phosphide phase.[26,29]

In the reversed scan, the SnP electrode displayed two peaks at 0.46 V and 0.7 V, which can be associated with gradual desodiation of the Na-Sn alloy phase.[26,60] In addition, the second peak at a higher potential, 0.7 V, can be assigned to desodiation of the sodium phosphide phase.[26,61] Upon further cathodic cycles, three peaks at 0.57 V, 0.23 V and 0.01 V appeared. The peak at 0.57 V was attributed to the reaction of phosphorous with sodium,[26,62] and the peaks at 0.23 V and 0.01 V to the gradual sodiaton of Sn.[61]

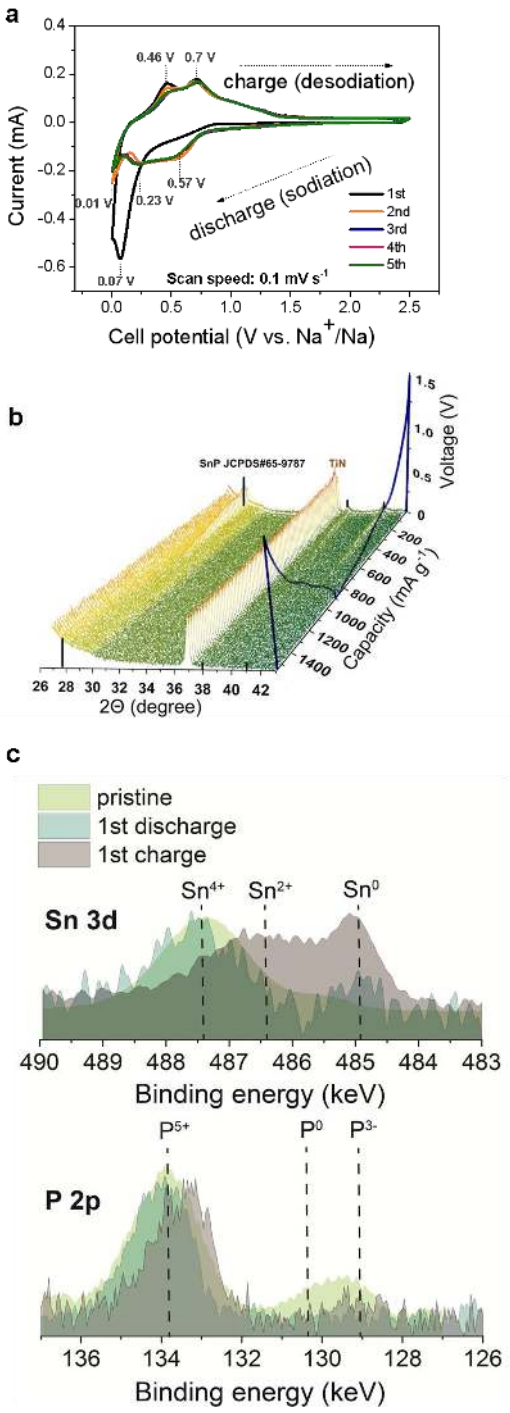

Fig. 5 a) Cyclic voltammetry curves of the initial five charge–discharge cycles for electrodes comprising SnP NCs (scan rate = 0.1 mV s^{-1}) measured using 5M NaFSI (sodium(I) bis(fluorosulfonyl)imide) in dimethoxyethane (DME) sodium electrolyte. b) Structure evolution of SnP NCs during electrochemical sodiation. In situ XRD patterns collected during the first discharge/charge of the SnP NCs using a current rate of 10 mAh g^{-1} in the potential range of 5 mV-1.5 V. c) *Ex-situ* XPS spectra of electrodes composed of SnP NCs before (pristine) and after discharge and charge. Prior measurements, the electrodes were rinsed from the Na electrolyte using pure dimethoxyethane solvent.

To identify the crystallographic phase evolution of the SnP electrode, in situ XRD analyses were performed (Fig. 5b). A steady decrease of the intensity of the SnP diffraction peaks and a concomitant peak broadening indicated that the sodiation of SnP NCs occurred with concominant amorphization of the material. After desodiation, the SnP trigonal structure was not recovered and the material remained amorphous. Previous works using Sn_4P_3 particles observed a metallic tin segregation during cycling, which was related to the anode performance deterioration.[25] No phase segregation was observed during the sodiation and desodiation of SnP in the present work from XRD analysis. SEM-EDX analysis of the initial SnP electrode and the same electrode after several cycles did not show evidences of significant phase segregation at the micron scale (Figure S16). However, segregation at the nanometer scale, into amorphous phases or very small and defective crystalline domains could be not discarded.

The sodiation/de-sodiation mechanism was interrogated also by *ex situ* XPS analysis for pristine, discharged and charged electrodes (Fig. S5c). After discharge, the Sn 3d peak position did not changed much in comparison with pristine sample. Upon charge, however, Sn 3d peak shifted towards lower binding energy indicating on the reduction of $Sn^{4+/2+}$ towards formation of metallic Sn. The peak of phosphorous at 129 eV corresponding to metal-P bond was fully vanished after discharge. For the following charge, the small shift of phosphorous peak at 133.8 eV corresponding to slight reduction of phosphorous from P^{5+} (phosphate chemical environment) toward lower oxidation state was observed.

As follows from CV and XPS measurements, the initial discharging process of SnP most likely takes place with formation of Na-Sn alloy and sodium phosphide phases. Upon following charge, SnP structure can not be recovered following formation of the mixture of elemental Sn and P (not visible from XPS spectra most probably due to the fast oxidation of phosphorous in ambient atmosphere).

To maximize the battery performance, both the anode material and the liquid electrolyte need to be optimized. Electrolytes based on $NaClO_4$, $NaPF_6$ and NaFSI salts were tested. Measuring the cycling performance of SnP anodes with the various sodium electrolytes, we concluded that the ultraconcentrated sodium electrolyte based on NaFSI in dimethoxyethane (DME) provided the highest stability (Fig. S17, S18). The enhanced electrochemical performance of SnP NCs with NaFSI electrolyte was attributed to the formation of a stable SEI that effectively suppress further electrolyte reduction during battery cycling.[58,59,63] NaFSI is actually the only electrolyte that, to a certain extent, can decrease sodium dendritic growth on Na metal during cycling.[55,56] This advantage is related to its improved SEI stability. In addition, NaFSI electrolyte has a high oxidation stability and ionic conductivity.[58]

Fig. 6a shows rate-capability measurements of Na-ion half-cells based on SnP NCs at various current densities of 0.05 – 2.5 A g^{-1} yielding capacities of 645 - 396 mAh g^{-1}, respectively. Importantly, when the current rate was set back to 50 mA g^{-1}

from the high current density of 2.5 A g^{-1}, almost full capacity recovery was measured. These results indicated a high electronic conductivity and charge-transfer kinetics in the SnP-based anode. As shown in the Fig. 6b, the voltage profiles during galvanostatic cycling were similar at all current densities. The galvanostatic curves were rather smooth, which suggest slow, gradual sodiation of SnP NCs.

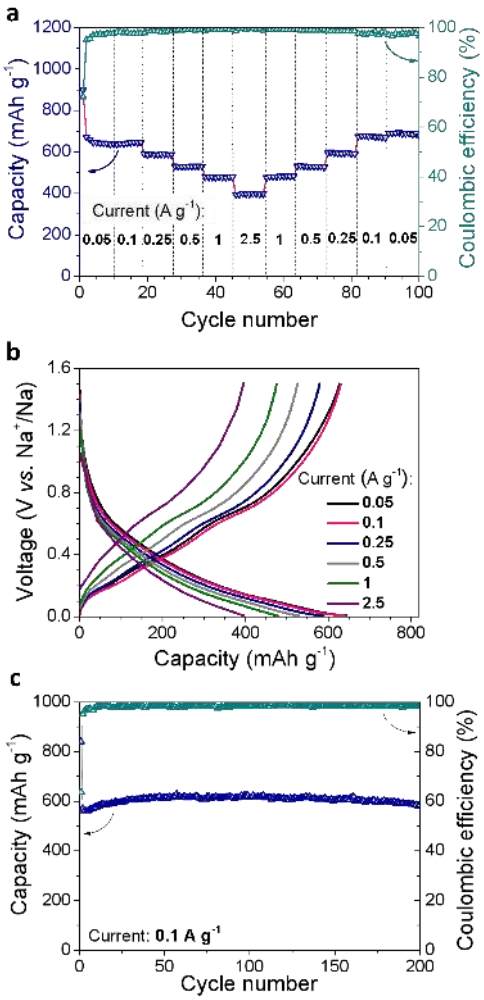

Fig. 6 Electrochemical performance of SnP NCs. Rate capability measurements (a), galvanostatic charge-discharge voltage curves (b) and cyclic stability of Na-ion half-cells employing SnP anodes made from SnP NCs at 0.1 A g^{-1} (c). All anodes had the same composition of SnP(64%)/CB(21%)/CMC(15%) and were cycled at room temperature at various current densities of 0.05 – 2.5 A g^{-1}; 5M NaFSI in DME solution was used as electrolyte for Na-ion cells. All batteries were cycled in the potential range of 5 mV - 1.5 V. The obtained capacities were normalized by the mass of SnP.

The cycling stability tests of half-cells employing SnP NCs at current densities of 0.1 A g^{-1} and 0.5 A g^{-1} showed high capacity retention over 200 and 500 cycles (Fig. 6c, S18, S19, S20) with high columbic efficiency of 98.3% and 99.0%. To the best of our knowledge, this is the longest cycle live demonstrated so far for tin phosphide-based anodes.[26,29,30,60,64] We attribute the high electrochemical cyclic stability demonstrated for SnP NC-based electrodes to two factors: i) the small size of the particles, which prevents them from accumulating sufficient stresses to mechanically disintegrate during sodiation and desodiation cycles; and ii) to the convenient crystal structure and composition of the NCs, which maintained the SnP phase without major segregation of tin and phosphorous during cycling.

Conclusions

To summarize, pure-phase SnP NCs were produced from the reaction of HMPT and a tin phosphonate obtained from tin oxalate and a long chain phosphonic acid. The tin precursor and the type and amount of phosphonic acid were key parameters to produce pure and highly crystalline tin monophosphide NCs. SnP NCs showed organized orientation of diphosphorous pairs within their layered crystal structure. SnP NCs were tested for the first time as anode material for SIBs. SnP NC-based SIB anodes exhibited specific capacity of about 600 mA h g^{-1} at a current density of 100 mA g^{-1} and very stable cycling performance with negligible capacity fading over 200 cycles. This excellent performance was attributed to the sodiation of the two components within the phosphide, the small size of the crystal domains and the proper phosphorous-rich composition.

Conflicts of interest

There are no conflicts of interest to declare.

Author Contributions

The manuscript was prepared through the contribution of all authors. K. K., M. M. and A. C. convinced and guided the project, and supervised the work. J. L. designed the experiments, produced the nanoparticles and wrote the manuscript. S. W., K. K., M. I., F. K., R. W. and M. V. K. performed the electrochemical measurements and wrote the battery part. D. N. and J. A. performed structural and compositional NCs characterization by means of HRTEM and EELS and discussed these results. J. L. measured and discussed XPS data. The manuscript was corrected and improved by all authors.

Acknowledgements

DN and JA acknowledge funding from Generalitat de Catalunya 2014 SGR 1638 and the Spanish MINECO projects VALPEC and ANAPHASE (ENE2017-85087-C3-3-R). ICN2 acknowledges support from the Severo Ochoa Programme (SEV-2013-0295) and is funded by Generalitat de Catalunya. JL thanks the China Scholarship Council for scholarship support. MM acknowledges a Juan de la Cierva formación grant by the Spanish MINECO.

Notes and references

1 W. Luo, F. Shen, C. Bommier, H. Zhu, X. Ji, L. Hu, *Acc. Chem. Res.* 2016, **49**, 231-240.
2 J. Y. Hwang, S. T. Myung, Y. K. Sun, *Chem. Soc. Rev.* 2017**, 46**, 3529-3614.
3 K. Nobuhara, H. Nakayama, M. Nose, S. Nakanishi, H. Iba, *J. Power Sources*, 2013, **243**, 585-587.
4 J. Cui, S. Yao, J. K. Kim, *Energy Storage Mater.*, 2017, **7**, 64-114.
5 Q. Xia, W. Li, Z. Miao, S. Chou, H. Liu, *Nano Res.*, 2017, **10**, 4055-4081.
6 F. Yang, H. Gao, J. Chen, Z. Guo, *Small Meth.*, 2017, **1**, 1700216.
7 D. H. Youn, H. Park, K. E. Loeffler, J. H. Kim, A. Heller, C. B. Mullins, *ChemElectroChem*, 2017, **4**, 1-7
8 Y. Kim, Y. Park, A. Choi, N. S. Choi, J. Kim, J. Lee, J. H. Ryu, S. M. Oh, K. T. Lee, *Adv. Mater.*, 2013, **25**, 3045-3049.
9 J. Qian, X. Wu, Y. Cao, X. Ai, H. Yang, *Angew. Chem.*, 2013, **52**, 4633-4636.
10 W. Li, S. Hu, X. Luo, Z. Li, X. Sun, M. Li, F. Liu, Y. Yu, *Adv. Mater.*, 2017, **29**, 1605820.
11 Z. Li, L. Zhang, X. Ge, C. Li, S. Dong, C. Wang, L. Yin, *Nano Energy*, 2017, **32**, 494-502.
12 M. Walter, M. I. Bodnarchuk, K. V. Kravchyk, M. V. Kovalenko, *Chimia (Aarau)*, 2015, **69**, 724-728.
13 W. J. Li, Q. R. Yang, S. L. Chou, J. Z. Wang, H. K. Liu, *J. Power Sources*, 2015, **294**, 627-632.
14 C. Wu, P. Kopold, P. A. Aken, J. Maier, Y. Yu, *Adv. Mater.*, 2017, **29**, 1604015.
15 J. Fullenwarth, A. Darwiche, A. Soares, B. Donnadieu, L. Monconduit, J. Mater. Chem. A, 2014, 2, 2050-2059.
16 S. Kim, A. Manthiram, *Chem. Commun.*, 2016, **52**, 4337-4340.
17 M. Fan, Y. Chen, Y. Xie, T. Yang, X. Shen, N. Xu, H. Yu, C. Yan, *Adv. Funct. Mater.*, 2016, **26**, 5019-5027.
18 W. J. Li, S. L. Chou, J. Z. Wang, H. K. Liu, S. X. Dou, *Chem. Commun.*, 2015, **51**, 3682-3685.
19 A. M. Elshahawy, C. Guan, X. Li, H. Zhang, H. Hu, H. Wu, S. J. Pennycook, J. Wang, *Nano Energy*, 2017, **32**, 494-502.
20 W. Zhang, M. Dahbi, S. Amagasa, Y. Yamada, S. Komaba, Electrochem. Commun., 2016, 69, 11-14.
21 W. Li, L. Ke, Y. Wei, S. Guo, L. Gan, H. Li, T. Zhai, H. Zhou, *J. Mater. Chem. A*, 2017, **5**, 4413-4420.
22 W. Qi, H. Zhao, Y. Wu, H. Zeng, T. Tao, C. Chen, C. Kuang, S. Zhou, Y. Huang, *Sci. Rep.*, 2017, **7**, 43582
23 Z. Li, J. Ding, D. Mitlin, *Acc. Chem. Res.*, 2015, **48**, 1657-1665.
24 Y. Kim, Y. Kim, A. Choi, S. Woo, D. Mok, N. S. Choi, Y. S. Jung, J. H. Ryu, S. M. Oh, K. T. Lee, *Adv. Mater.*, 2014, **26**, 4139-4144.
25 D. Lan, W. Wang, l. Shi, Y. Huang, L. Hu, Q. Li, *J. Mater. Chem. A*, 2017, **5**, 5791-5796.
26 J. Qian, Y. Xiong, Y. Cao, X. Ai, H. Yang, *Nano Lett.*, 2014, **14**, 1865-1869.
27 Q. Li, Z. Li, Z. Zhang, C. Li, J. Ma, C. Wang, X. Ge, S. Dong, L. Yin, *Adv. Energy Mater.*, 2016, **6**, 1600376
28 J. Liu, P. Kopold, C. Wu, P. Aken, J. Maier, Y. Yu, *Energy Environ. Sci.*, 2015, **8**, 3531-3538.
29 W. Li, S. L. Chou, J. Z. Wang, J. H. Kim, H. K. Liu, S. X. Dou, *Adv. Mater.*, 2014, **26**, 4037-4042.
30 X. Fan, J. Mao, Y. Zhu, C. Luo, L. Suo, T. Gao, F. Han, S. Liou, C. Wang, *Adv. Energy Mater.*, 2015, **5**, 1500174
31 Y. Xu, B. Peng, F. M. Mulder, *Adv. Energy Mater.*, 2018, **8**, 1701847
32 L. Ma, P. Yan, S. Wu, G. Zhu, Y. Shen, *J. Mater. Chem. A*, 2017, **5**, 16994-17000.
33 S. Huang, C. Meng, M. Xiao, S. Ren, S. Wang, D. Han, Y. Li, Y. Meng, *Sust. Energy Fuels*, 2017, **1**, 1944-1949.
34 X. Fan, T. Gao, C. Luo, F. Wang, J. Hu, C. Wang, *Nano Energy*, 2017, **38**, 350-357.
35 J. Mao, X. Fan, C. Luo, C. Wang, *ACS Appl. Mater. Interfaces*, 2016, **8**, 7147-7155.
36 T. Kim, K. Hong, D. Sohn, M. Kim, D. Nam, E. Cho, H. Kwon, *J. Mater. Chem. A*, 2017, **5**, 20304-20315.
37 Y. Cheng, J. Huang, R. Li, Z. Xu, L. Cao, H. Ouyang, J. Li, H. Qi, C. Wang, *Electrochim. Acta*, 2015, **180**, 227-233.
38 D. Nam, T. Kim, K. Hong, H. Kwon, *ACS Nano*, 2014, **8**, 11824-11835.
39 L. Baggetto, P. Ganesh, R. P. Meisner, R. R. Unocic, J. Jumas, C. A. Bridges, G. M. Veith, *J. Power Sources*, 2013, **234**, 48-59.
40 C. Kim, K. Lee,, I. Kim, J. Park, G. Cho, K. Kim, J. Ahn, H. Ahn, *J. Power Sources*, 2016, **317**, 153-158.
41 M. F. Oszajca, M. I. Bodnarchuk, M. V. Kovalenko, *Chem. Mater.*, 2014, **26**, 5422-5432.
42 Q. Wang, C. Zhao, Y. Lu, Y. Li, Y. Zheng, Y. Qi, X. Rong, L. Jiang, X. Qi, Y. Shao, D. Pan, B. Li, Y. S. Hu, L. Chen, *Small*, 2017, **13**, 1701835
43 A. Standing, S. Assali, L. Gao, M. A. Verheijen, D. V. Dam, Y. Cui, P. H. Notten, J. E. Haverkort, E. P. Bakkers, *Nat. Commun.*, 2015, **6**, 7824.
44 J. Sun, C. Liu, P. Yang, *J. Am. Chem. Soc.*, 2011, **133**, 19306-19309.
45 N. Kornienko, D. D. Whitmore, Y. Yu, R. L. Stephen, P. Yang, *ACS Nano*, 2015, **9**, 3951-3960.
46 S. Tamang, C. Lincheneau, Y. Hermans, S. Jeong, P. Reiss, *Chem. Mater.*, 2016, **28**, 2491-2506.
47 A. Hitihami-Mudiyanselage, K. Senevirathne, S. L. Brock, *ACS Nano*, 2013, **7**, 1163-1170.
48 P. C. Donohue. H. S. Young, *J. Solid State Chem.*, 1970, **1**, 143-149.
49 V. Tallapally, R. J. A. Esteves, L. Nahar, I. U. Arachchige, *Chem. Mater.*, 2016, **28**, 5406-5414.
50 T. P. Sushkova, E. U. Kononova, Y. A. Savinova, E. S. Dorokhina, G. V. Semenova, *Condens. Matter. Inter.*, 2014, **16**, 210-214. (in russian).
51 J. Gullman, *J. solid state Chem.*, 1990, **87**, 202-207.
52 Y. Kim, H. Hwang, C. S. Yoon, M. G. Kim, J. Cho, *Adv. Mater.*, 2007, **19**, 92-96.
53 H. Liu, J. S. Owen, A. P. Alivisatos, *J. Am. Chem. Soc.*, 2007, **129**, 305-312
54 J. S. Owen, J. Park, P. Trudeau, A. P. Alivisatos, *J. Am. Chem. Soc.* 2008, **130**, 12279-12281
55 Z. A. Peng, X. Peng, *J. Am. Chem. Soc.*, 2001, **123**, 1389-1395
56 F. Hulliger, Structural Chemistry of Layer-Type Phases. Dordrecht, Holland, 1976, pp. 145.
57 J. F. Moulder, W. F. Stickle, P. E. Sobol, K. D. Bomben, Handbook of X-ray photoelectron spectroscopy, Perkin-Elmer, 1992, pp. 58–59.
58 J. Lee, Y. Lee, J. Lee, S. M. Lee, J. H. Choi, H. Kim, M. S. Kwon, K. Kang, K. T. Lee, N. S. Choi, *ACS Appl. Mater. Inter.*, 2017, **9**, 3723-3732.
59 K. Takada, Y. Yamada, E. Watanabe, J. H. Wang, K. Sodeyama, Y. Tateyama, K. Hirata, T. Kawase, A. Yamada, *ACS Appl. Mater. Inter.*, 2017, **9**, 33802-33809.
60 L. T. Zheng, R. A. Dunlap, M. N. Obrovac, *J. Electrochem. Soc.* 2016, **163**, A1188-A1191.
61 Z. J. Du, R. A. Dunlap, M. N. Obrovac, *J. Alloy. Compd.*, 2014, **617**, 271-276.
62 M. Dahbi, N. Yabuuchi, M. Fukunishi, K. Kubota, K. Chihara, K. Tokiwa, X. F. Yu, H. Ushiyama, K. Yamashita, J. Y. Son, Y. T. Cui, H. Oji, S. Komaba, *Chem. Mater.*, 2016, **28**, 1625-1635.
63 L. Schafzahl, I. Hanzu, M. Wilkening, S. A. Freunberger, *ChemSusChem*, 2017, **10**, 401-408.
64 H. Usui, Y. Domi, K. Fujiwara, M. Shimizu, T. Yamamoto, T. Nohira, R. Hagiwara, H. Sakaguchi, *ACS Energy Lett.*, 2017, **2**, 1139-1143.

TOC graphical abstract